Effects processing parameters and building orientation on the microstructural and mechanical properties of AlSi10Mg parts printed by selective laser melting

C. Phetolo*[1], V. Matjeke[1], and J. van der Merwe[1]

*Paper written on project work carried out in partial fulfilment of BTech (Metallurgical Engineering) degree

Affiliation:
[1]School of Chemical and Metallurgical Engineering, Faculty of Engineering and the Built Environment, University of the Witwatersrand, Johannesburg, South Africa.

Correspondence to:
J. van der Merwe

Email:
josias.vandermerwe@wits.ac.za

Dates:
Received: 12 Mar. 2021
Revised: 20 Jul. 2021
Accepted: 20 Jul. 2021
Published: July 2021

How to cite:
Phetolo, C., Matjeke, V., and van der Merwe, J. 2021 Effects processing parameters and building orientation on the microstructural and mechanical properties of AlSi10Mg parts printed by selective laser melting. Journal of the Southern African Insitute of Mining and Metallurgy, vol. 121, no. 7, pp. 345–350

DOI ID:
http://dx.doi.org/10.17159/2411-9717/1575/2021

ORCID:
J. van der Merwe
https://orcid.org/0000-0003-4563-8078

Synopsis

The mechanical properties and microstructure of AlSi10Mg alloy samples that were printed by selective laser melting (SLM) were studied to determine the effect of processing parameters and building orientation. After printing, the alloy was stress relieved at 250°C for 2 hours. The microstructures were analysed by optical microscopy and scanning electron microscopy (SEM) to determine the alloy phases and distribution. Phase transformation characteristics of the material were evaluated using differential scanning calorimetry (DSC). Mechanical properties were determined by subjecting the XY- and Z-built samples to tensile and nano-indentation testing. The samples from the tensile tests were then used to perform fractographic analysis by SEM. The microstructural properties in each orientation revealed a non-homogeneous microstructure which was characterized by a semi-elliptical tract and fine silicon precipitates, which were found to be softer along the fusion zone. The DSC thermograms revealed that the material underwent two phase transformations during the first heating cycle. The mechanical properties revealed a higher UTS, higher yield strength, and a lower percentage elongation in the Z orientation than in the XY orientation. Fractographic analysis showed that crack initiation in both orientations started from the surface in a brittle manner due to surface flows, and then propagated via microvoid coalescence.

Keywords
AlSi10Mg alloy, additive manufacturing, mechanical propeerties, microstructure.

Introduction

AlSi10Mg is an aluminum alloy that is often used in the fabrication of objects with complex shapes and with thin walls. Its widespread use is due to its exceptional hardness, strength, and dynamic properties (EOS, 2014). These properties make AlSi10Mg ideal for applications in the aerospace, automobile, and electronics industries, where a superior strength to weight ratio and thermal properties are required. Due to these ideal properties, considerable research is being done on how to use the alloy in additive manufacturing (AM), which is a fabrication process used to print 3D objects. The process is carried out by printing successive layers of material until a complete 3D object, pre-defined in the computer aided device (CAD) file, is built (Ngo, 2018).

The purpose of this study was to determine the effect of building orientation and processing parameters on the mechanical properties of AlSi10Mg samples derived by AM. The build orientation has been investigated by several authors; however, the combination of building direction and processing parameters has not been fully explored (Matjeke *et al.*, 2020; Mfusi *et al.*, 2018). AM is gaining considerable commercial acceptance because it enables the fabrication of complex shapes with good precision (Srivatsan, Manigandan, and Sudarshan, 2015). It is preferred over conventional fabrication processes like casting and deformation processes because it does not require new tools or moulds during the production of prototypes and customized parts, thus leading to lower production costs and lead times (Srivatsan, Manigandan, and Sudarshan, 2015).

Effects processing parameters and building orientation

One of the main drawbacks of the casting process when compared to AM is the inability to produce repeatable results due to process-related defects such as porosity and inclusions (du Plessis *et al.*, 2019; Girelli *et al.*, 2019). This can be combated by optimizing process parameters like the building direction, which is essentially the orientation of material accumulation during fabrication (Qin *et al.*, 2019).

There is a vast pool of building directions from which to pick, including the Y, Z, XY, X, and 45° orientations. The building orientation direction chosen affects support structure production, building cost, tool path planning, and building time, as well as the microstructure and mechanical properties of the printed component (Li *et al.*, 2016; Qin *et al.*, 2019). As a result, it is critical to choose a building direction that will result in desirable mechanical properties, a homogeneous microstructure, and negligible flaws at a fair cost.

Materials and experimental procedure

A 280 HL selective laser melting (SLM) platform with a bed size of 280 × 280 × 350 mm was used to produce the alloy test samples from AlSi10Mg alloy powder. Tensile specimens were produced ready for testing and no machining was performed prior to testing. Metal part geometry was fabricated directly from the computer aided design (CAD), using the the manufacturing parameters outlined in Table I. The widely used volume-based energy density E (J/mm^3) is defined in Equation [1]:

$$E = \frac{P}{vhl} \quad [1]$$

where P is laser power (W), v is scan speed (mm/s), h is hatch spacing (mm), and l is the layer thickness.

The samples were heat-treated at 250°C for 2 hours in a furnace in order to stress-relieve the as-built components after the SLM process.

Characterization

A Microtrac laser particle size analyser and a Zeiss Merlin field emmission scanning electron microscope were used to determine the powder particle size distribution and the morphology respectively. The environment in the build chamber was kept inert by purging with argon gas at a flow rate of 0.3 l/min. Differential scanning calorimetry (DSC) was carried out to determine the exact critical transformation temperature and the enthalpy required to melt the powder. DSC testing and processing parameters are shown in Table II. Samples for metallographic examination were prepared by transversely sectioning the tensile test samples. The sectioned samples were mounted and polished using suspensive lubrication and 3 µm and 1 µm polishing cloths, with a 0.5 µm colloidal finish. The samples were then etched using a solution consisting of 1% HF, 1% HCl, and 2.5% HNO_3 and examined by optical and electron microscopy.

Table I

SLM process parameters

Parameter	This work	Tang and Pistorius (2017)	Mfusi *et al.*, 2018
Laser power (W)	370	370	150
Scanning speed (mm/s)	1000	1300	1000
Hatch spacing (µm)	180	100	50
Scanning strategy	Stripes	Stripes	Stripes
Layer thickness (µm)	30	30	50

Table II

DSC processing parameters

Parameter	Value
Heating rate (°C/min)	100
Sample mass (mg)	13.77
Argon gas flow rate (ml/min)	100

Mechanical testing

All samples were prepared and tested in accordance with ASTM E8/E8M. Tensile tests were performed with an MTS Landmark servo-hydraulic test system using samples with a gauge length of 150 mm and diameter of 12.5 mm. The samples were were pulled at a rate of 0.8 mm/s at room temperature until fracture. An extensometer was used during the test, and the slope of the elastic region on the flow stress curve was measured and used to calculate the Young's modulus. Hardness tests were carried out on a Brinell hardness tester at a load of 62.5 kg force using 1 mm diameter for 10 seconds. Nano-indentation tests were carried out on additional etched samples to examine the different phases in the microstructure, using a three-sided pyramidal Berkovich diamond indenter.

Results

Particle size distribution and morphology

The particle size distribution is summarized in Figure 1. The d_{50} of the distribution was found to be 43.89 µm, with the majority of the particles concentrated about the mean.

Visual inspection confirmed the particle size distribution, the sample being dominated by large particles with a few smaller particles. Figure 2 shows that the combination of large particles and small particles resulted in a high degree of compaction. The majority of the particles were close to spherical. Some of the particles with irregular shapes were formed when small particles attached to larger spherical particles, and others were originally irregular shapes. The chemical composition of the as-built AlSi10Mg alloy is presented in Table III.

Metallography

The microstructure of the samples built in the XY (horizontal) direction shows a semi-elliptical, or slightly parabolic, morphology as shown in Figure 4A. The dimensions of the

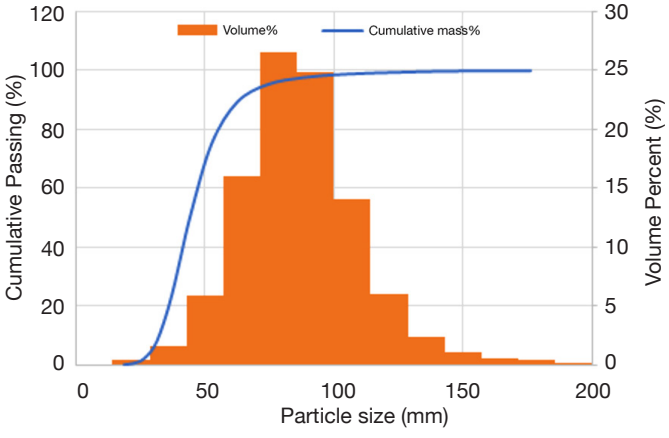

Figure 1—Particle size distribution of the powder used for SLM

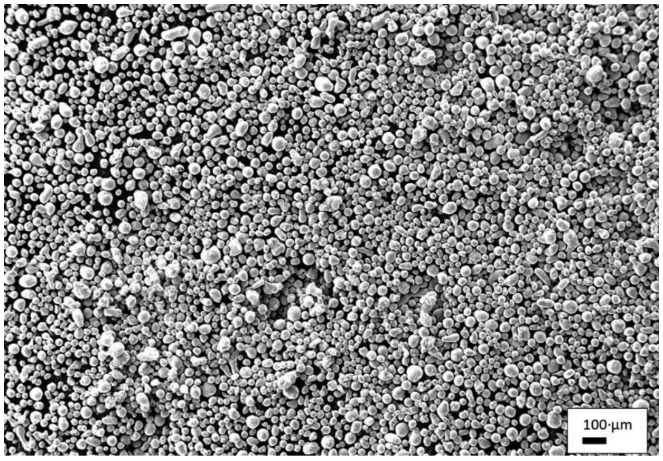

Figure 2—AlSi10Mg powder at low magnification (100×)

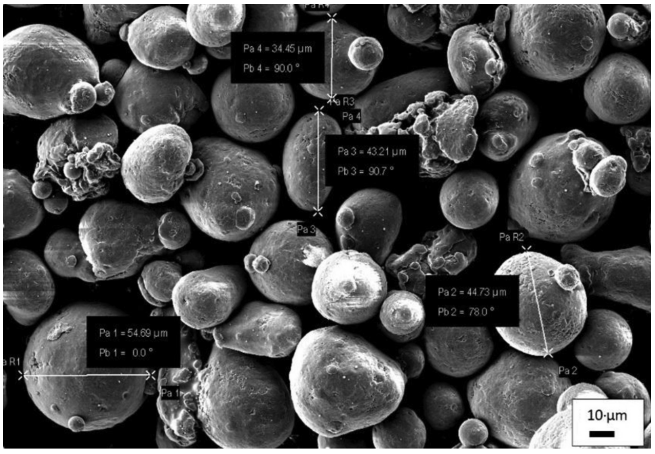

Figure 3—AlSi10Mg powder at higher magnification, indicating particle morphology

Table III

Chemical composition of the AlSi10Mg alloy (wt%), as determined by EDS analysis

Al	Si	Mg	O
89.3	9.8	0.6	0.3

semi-elliptical tracks were measured using the ImageJ analyser software. The measured semi-elliptical tracks presented in Figure 5 had an average width of 60 µm. The microstructure of the sample built in the Z (build) direction (Figure 6) also demonstrated a semi-elliptical morphology and spacing with an average width of 110 µm. However, it must be noted that because of overlap the track width cannot be determined from the interior of builds and the estimates of 60 and 110 µm are clearly too small, since the hatch spacing was 180 µm. The coarse silicon phase was also observed at higher magnifications, like in the XY (horizontal) direction shown in Figure 4D. The semi-elliptical

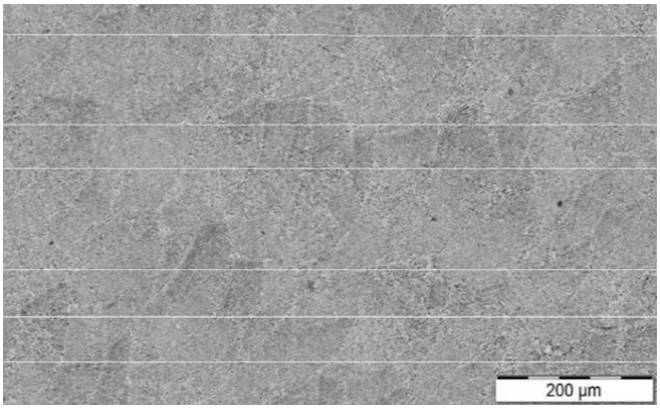

Figure 5—XY-direction microstructure showing grain size analyses

tract in the Z (or build) direction appears flatter than that in the XY orientation. The microstructure in both the XY and Z

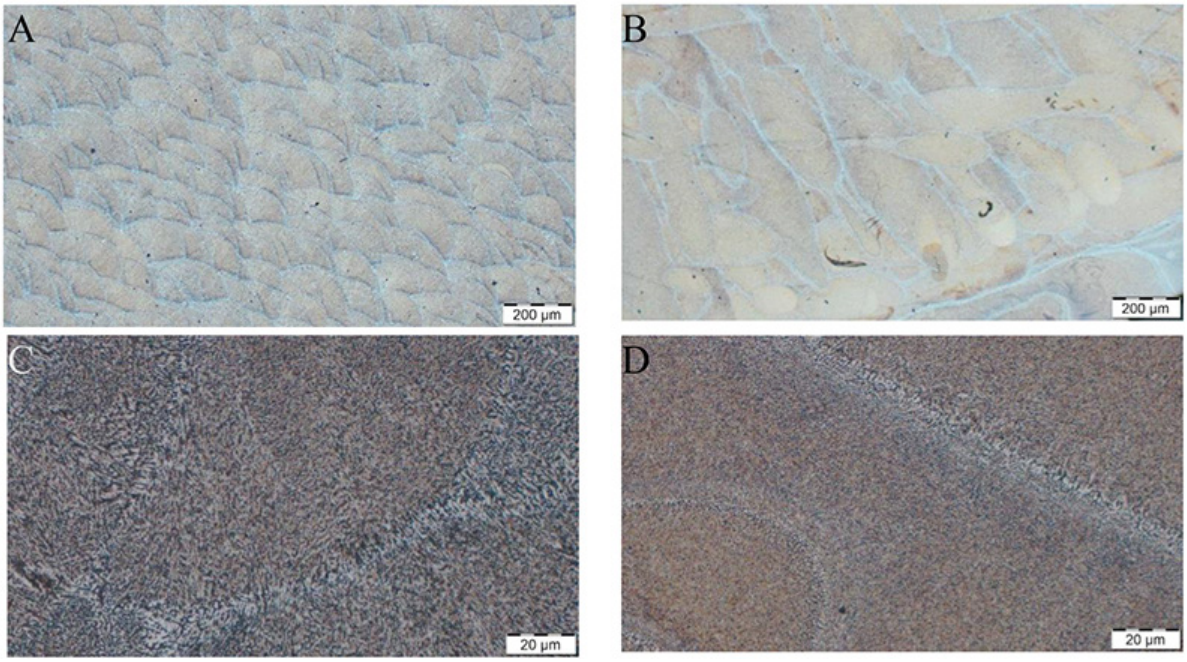

Figure 4—Microstructures A and C represent the low and high magnifications of direction XY respectively, while, microstructures B and D represent the low and high magnifications of direction Z respectively

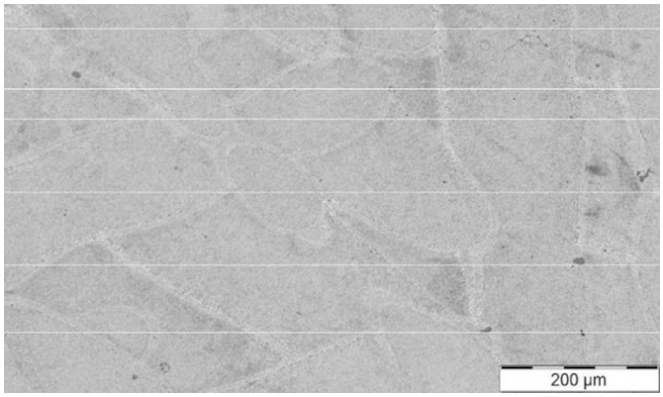

Figure 6—Z-direction microstructure showing grain size analyses

direction comprises coarse and fine areas. The size of the of the precipitates decreases towards the centre of the semi-elliptical track.

At higher magnifications, the focus is inside the core of the elliptical track of the microstructure. Figure 7 indicates a cellular pattern, which is a result of silicon particles forming an interconnected fine network surrounding the Si-rich aluminum matrix. The region highlighted within the black lines shows an area with a slightly coarser microstructure located at the melt pool boundary. At even higher magnification the microstructure shows second-phase precipitates as light grey particles within the darker grey matrix, as indicated in Figure 8.

Calorimetry

The calorimetric results are presented in Figure 9. The thermogram is characterized by two exothermic peaks at temperatures of 567.4°C and 687.3°C. These peaks represent the critical transformation temperature and melting point of AlSi10Mg. The first exothermic peak is followed by an endothermic peak at a maximum temperature of 604.6°C. The DSC measurements provided the exact properties that are associated with AlSi10Mg. This information can be useful during optimization of the processing parameters and during selection of a heat treatment process. However, the peaks occur at a considerably higher temperature than previously reported (Fiocchi *et al.*, 2016). The thermogram also revealed an endothermic peak which starts at around the melting temperature of AlSi10Mg, which is 570°C, and therefore represents the melting of the sample.

Mechanical test results

Tensile properties

The tensile test results are summarized in Table V. The deformation characteristic and flow curves are presented in Figure 10. More than one samples was tested, but only the representative curves are shown, and although there was no slip in the jaws some of the samples showed a jagged edge during the initial stage of the test. The Z build orientation exhibited higher strength than the XY orientation.

The modulus of elasticity for the XY orientation was 41 GPa, with the yield point in the region of 200 MPa at a strain of 0.006. The modulus of elasticity for the Z direction was 40 GPa, with the elastic limit being reached at 209 MPa and a strain of 0.008. The deformation behaviour in both orientations along the elastic region is comparable, and major difference start

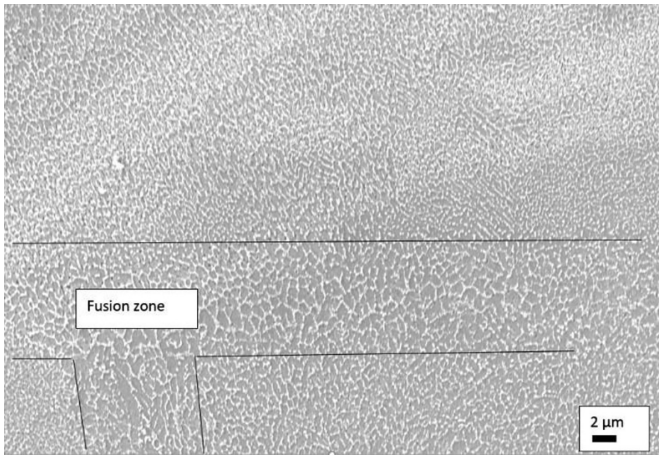

Figure 7—Microstructure of AlSi10Mg printed by SLM

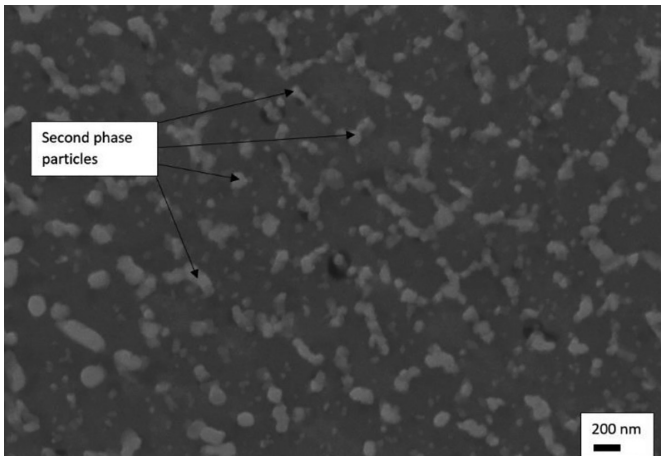

Figure 8—Microstructure of AlSI10Mg indicating the presence of second-phase particles

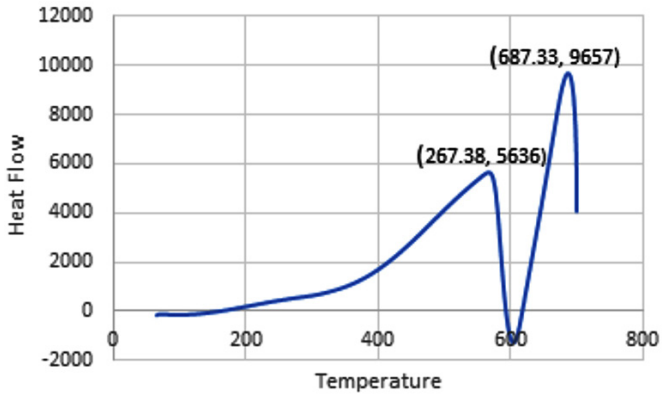

Figure 9—DSC thermogram of AlSi10M

to appear after the commencement of plastic deformation. The ultimate tensile strength (UTS) recorded for the XY orientation was 294 MPa, with the fracture point being reached after an elongation of 8.17%. The Z orientation recorded a UTS of 324 MPa, with fracture taking place after 5.9% elongation. The results of the tensile tests are summarized in Table V. The tests revealed that the XY orientation showed better ductility than the Z orientation. The higher ductility in the XY orientation came as

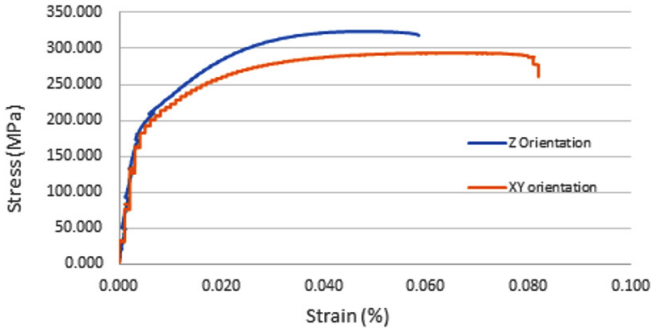

Figure 10—Engineering stress *vs* strain curves for Z and XY orientations

a trade-off for strength, as the Z orientation showed higher yield strength and UTS. Nahmany *et al.* (2019) and Tang and Pistorius (2017) also reported a lower percentage elongation and a higher UTS for the Z orientation; however, the higher yield strength reported in this work for the Z orientation is contrary to previous findings.

Hardness

The average Brinell hardnesses and nano-indentation results are summarized in Tables VI and VII. The general measurement revealed that the harness is less in the XY orientation than the Z orientaton. Nano-indentation hardness was investigated to determine the properties of each phase, and it was found that the Al matrix was softer than the Si precipitates, as shown in Table VII.

Si particles recorded the highest hardness at 608 HV, while the core of the semi-elliptical track recorded the second highest hardness of 144 HV. The fusion zone, which comprised the heat-affected zone (HAZ) region (the semi-elliptical core) recorded 104 HV, while the matrix recorded the lowest hardness at 113 HV. The Young's modulus results mirror the hardness results along the different phases, with the Si particles recording 166 GPa followed by the fusion zone, semi-elliptical core, and matrix at 85 GPa, 80 GPa, and 68 GPa respectively.

Discussion

Based on the results of this study and other work, it seems that the combination of processing parameters and building direction affects the mechanical properties (Mfusi *et al.*, 2018). Although Mfusi *et al.* did not conduct tensile tests on stress-relieved samples, an inference and pattern can be drawn from the as-built- tensile test results. Aboulkhair *et al.* (2016) reported that AlSi10Mg components printed by SLM owe their strength to three main factors: grain boundary strengthening, solid solution strengthening, and interaction of dislocations. The grain boundary strengthening in both the XY and Z orientation is due to the fine silicon microstructure, which is a result of rapid cooling during the printing process. The solid solution strengthening is provided by the silicon particles, which are rejected from the supersaturated aluminum matrix during heat treatment to form a Si-rich phase throughout the sample, but mostly concentrated along the cellular boundaries, and is which coarser on the melt pool boundaries rather than on the semi-elliptical core.

The non-homogeneous microstructure was further investigated by performing nano-indentation tests to determine the nano-mechanical properties of different phases in the microstructure. The results from the nano-indentations seemed to contradict the findings of the microstructural analysis. The nano-indentation hardness results indicated that the fusion zone is harder than the semi-elliptical core, while the microstructural analysis showed that the semi-elliptical core has a finer microstructure and would thus be expected to be harder than the fusion zone. The Si particles had the highest hardness, and this would allow them to act as second-phase particles and strengthen the alloy via solid solution strengthening.

Table VI

Vickers hardness results

Orientation	Average hardness (HB)
XY 90+1 Z 94+1	

Table VII

Microhardness and Young's modulus results

	Fusion zone	Semi-elliptical core	Matrix	Si particle
Nano-ndentation) Young's modulus (GPa)	104 80	144 85	113 68	608 166

Conclusion

It can be concluded that processing parameters and building direction should be considered together in order to optimize the mechanical properties of SLM-printed AlSi10Mg parts. Although the stress-relief process conducted in this investigation differed from the heat treatment used by Tang and Pistorius (2017) and Mfusi *et al.* (2018), an inference can be drawn from the pattern. The manufacturing process resulted in a non-homogenous microstructure in which different regions, such as the matrix, semi-elliptical core, and fusion zone were found, as well as Si-rich second-phase particles in both the Z and XY orientations. The rejection of Si from the supersaturated matrix was confirmed by the exothermic peaks in the thermograms. The Z orientation showed better mechanical properties, with a higher UTS and yield strength but lower ductility compared to the XY orientation. Therefore, it can be concluded that for applications that require a material with high strength, the components should be printed in the Z orientation, and for cases where high ductility is required and high strength is not a primary requisite, the components can be built in the XY orientation.

Table V

Tensile test results

	This work			Tang and Pretorius (2017)			Mfusi *et al.*, (2018)		
	YS (MPa)	UTS (MPa)	%E	YS (MPa)	UTS (MPa)	%E	YS (MPa)	UTS (MPa)	%E
XY 200 Z 209	294 324	8.2 5.9	182 180	285 287	17.9 14.3	264 244	460 473	6.3 6.8	

References

Aboulkhair. N.T., Maskery. I., Tuck. C., Ashcroft. I., and Everitt. N.M. 2016. Improving the fatigue behaviour of a selectively laser melted aluminium alloy: Influence of heat treatment and surface quality. *Materials & Design*, vol. 104. pp. 174–182.

Du Plessis, A. Glaser, D., Moller, H., and Mathe, N. 2019. Pore closure effect of laser shock peening of additively manufactured AlSi10Mg. *3D Printing and Additive Manufacturing*, vol. 6, no. 5. pp. 245–252. doi: 10.1089/3dp.2019.0064

EOS. 2014. Material data sheet: Aluminium alloy AlSi10Mg. EOS GmbH. https://www.eos.info/03_system-related-assets/material-related-contents/metal-materials-and-examples/metal-material-datasheet/aluminium/material_datasheet_eos_aluminium-alsi10mg_en_web.pdf [accessed 7 June 2021].

Fiocchi,. J., Tuissi,. A., Bassani,. P., and Biffi,. C.A. 2016. Low temperature annealing dedicated to AlSi10Mg selective laser melting products. *Journal of Alloys and Compounds*, vol. 695. doi: 10.1016/j.jallcom.2016.12.019

Girelli, L., Tocci, M., Gelfi, M., and Pola, A. 2019. Study of heat treatment parameters for additively manufactured AlSi10Mg in comparison with corresponding cast alloy. *Materials Science & Engineering A*, vol. 739. pp. 317–328. doi: 10.1016/j.msea.2018.10.026

Li, W., Li, S., Zhamg, A., Zhou, Y., Wei, Q., Yan, C., and Shi, Y. 2016. Effect of heat treatment on AlSi10Mg alloy fabricated by selective laser melting : Microstructure evolution, mechanical properties and fracture mechanism', *Materials Science & Engineering A*, vol. 663. pp. 116–125. doi: 10.1016/j.msea.2016.03.088

Matjeke, V., Moopanar, C., Bolokang, A.S., and van der Merwe, J.W. 2020. Effect of heat treatment on the microstructure and mechanical deformation behavior of additive-manufactured AlSi10Mg components. *Progress in Additive Manufacturing*, vol. 5. pp. 379–385. doi: 10.1007/s40964-020-00139-1

Mfusi, B.J., Tshabalala, L.C., Popoola, A.P.I., and Mathe, N.R. 2018. The effect of selective laser melting build orientation on the mechanical properties of AlSi10Mg parts. *IOP Conference Series: Materials Science and Engineering*, vol. 430. Conference of the South African Advanced Materials Initiative (CoSAAMI-2018), Vanderbijlpark, South Africa, 23–26 October 2018. doi: 10.1088/1757-899X/430/1/012028

Nahmany, M., Hadad, Y., Aghion, E., Stern, A., and Frage, N. 2019. Microstructural assessment and mechanical properties of electron beam welding of AlSi10Mg specimens fabricated by selective laser melting. *Journal of Materials Processing Technology*, vol. 270. pp. 228–240.

Ngo, T.D., Kashani, A., Imbalzano, G., Nguyen, K.T.Q., and Hui, D. 2018. Additive manufacturing (3D printing): A review of materials, methods, applications and challenges. *Composites Part B: Engineering*, vol. 143. pp. 172–196. https://doi.org/10.1016/j.compositesb.2018.02.012

Qin, Y., Qi, Q., Scott, P.J., and Xiangqian, J. 2019. Determination of optimal build orientation for additive manufacturing using Muirhead mean and prioritised average operators. *Journal of Intelligent Manufacturing*, vol. 30. pp. 3015–3034. https://doi.org/10.1007/s10845-019-01497-6

Srivatsan, S.T., Manigandan, K., and Sudarshan, S.T. 20115. Additive manufacturing of materials: viable techniques. *Additive Manufacturing. Innovations, Advantages, and Applications*. Srivatsan, T.S. and Sudarshan, T.S. (eds). CRC Press, Boca Raton, FL. pp. 1–48. https://doi.org/10.1201/b19360

Tang, M. and Pistorius, P.C. 2017. Oxides, porosity and fatigue performance of AlSi10Mg parts produced by selective laser melting. *International Journal of Fatigue*, vol. 94. pp. 192–201. ◆